Shear modulus reconstruction in dynamic elastography: time harmonic case

Eunyoung Park and Antoinette M Maniatty

Department of Mechanical, Aerospace and Nuclear Engineering, Rensselaer Polytechnic Institute, Troy, New York 12180, USA

E-mail: parke@rpi.edu and maniaa@rpi.edu

Abstract

This paper presents a direct inversion approach for reconstructing the elastic shear modulus in soft tissue from dynamic measurements of the interior displacement field during time harmonic excitation. The tissue is assumed to obey the equations of nearly incompressible, linear, isotropic elasto-dynamics in harmonic motion. A finite element discretization of the governing equations is used as a basis, and a procedure is outlined to eliminate the need for boundary conditions in the inverse problem. The hydrostatic stress (pressure) is also reconstructed in the process, and the effect of neglecting this term in the governing equations, which is common practice, is considered. The approach does not require iterations and can be performed on sub-regions of the domain resulting in a computationally efficient method. A sensitivity study is performed to investigate the detectability of abnormal regions of different size and shear modulus contrast from the background. The algorithm is tested on simulated data on a two-dimensional domain, where the data are generated on a very fine mesh to get a near exact solution, then downsampled to a coarser mesh that is similar to the spatial discretization of actual data, and noise is added. Results showing the effect of the hydrostatic stress term and noise are presented. A reconstruction using MR measured experimental data involving a tissue-mimicking phantom is also shown to demonstrate the algorithm.

(Some figures in this article are in colour only in the electronic version)

1. Introduction

Tissue stiffness is closely related to the pathology of the tissue and thus detecting abnormalities in tissue stiffness is a valuable diagnostic tool. Palpation is a long-standing, standard medical practice which is used to assess stiffness variations in accessible regions of soft tissue to detect abnormalities, such as tumours. However, if the abnormal tissue is too small and/or is located

3697

deep inside the body, inaccessible from the body surface, palpation is not an effective detection method. Diagnostic imaging modalities such as ultrasound, magnetic resonance imaging (MRI) and x-ray computed tomography have been used to estimate other pathological changes in tissue more quantitatively. In general, however, some kinds of lesions may not have the properties which make them detectable using conventional modalities. Such cases include the cirrhosis of the liver and tumours of the prostate and breast (Ophir *et al* 1991). For example, a tumour in the breast may appear normal in conventional ultrasound, since the difference of the echogenic property between the normal and the abnormal tissues may be insignificant. However, the tumour is much stiffer than the surrounding tissue making it readily detectable by palpation if it is sufficiently large and near the surface. Furthermore, the elastic properties of tissues are directly related to their underlying structure, i.e. their molecular building blocks and the structural organization of these blocks (Fung 1981). In particular, it is the elastic resistance to shape change, characterized by the shear modulus (neglecting anisotropy), that is most affected by pathological changes in tissue. Thus, imaging the shear modulus has the potential to provide high contrast images that differentiate between various pathological states of the tissue. For example, the shear modulus in breast cancer is typically 7 to 28 times stiffer than normal tissue (Sarvazyan 1993, Walz *et al* 1993, Krouskop *et al* 1998) and about 8 times stiffer than benign fibroadenomas (Walz *et al* 1993). Thus, the imaging of the elastic shear modulus holds great promise for early diagnosis of pathological abnormalities in soft tissue, particularly in cases where the lesion is small or in an inaccessible region, not readily detectable by palpation.

In elastography (a term coined by Ophir *et al* (1991)), the mechanical response of tissue, typically the displacement field, is recorded in response to an applied force or motion. Several groups use ultrasound to measure the displacement field as a function of space and time in response to different types of tissue excitations, such as quasi-static compression (elastography), see for example the work of Ophir and co-workers (Ophir *et al* 1991, Konofagou *et al* 1998, Ophir *et al* 2000, Srinivasan *et al* 2004), low frequency vibration (sonoelastography), see for example the work of Parker and co-workers (Lerner *et al* 1988, Parker *et al* 1990, Wu *et al* 2002, Taylor *et al* 2004), and single pulsed, low frequency excitation (transient elastography), see for example the work of Fink and co-workers (Catheline *et al* 1999, 2000, Tanter *et al* 2002, Bercoff *et al* 2003). In the quasi-static case, a pressure induced strain is calculated by comparing standard ultrasonic images of tissue before and after compression, and this spatial strain information is either imaged directly or related to the elastic stiffness which is then imaged. A principle drawback of static data is that, without knowledge of stress boundary conditions, the elastic modulus cannot be uniquely reconstructed (Barbone and Bamber 2002). For this reason, the present work focuses on considering dynamic excitations. In the low frequency vibration case, a standard Doppler ultrasound technique is used to measure the motion induced by harmonic excitation. In the single pulse excitation case, a low frequency, single pulse is used to stimulate the tissue, and the displacement data are recorded with a specially designed and built high speed ultrasound system. Using a phase contrast magnetic resonance (MR) technique, it is also possible to image tissue motion in response to a mechanical excitation, referred to as magnetic resonance elastography (MRE); see, for example, the works of (Muthupillai *et al* 1995, Van Houten *et al* 2003, McKnight *et al* 2002). In that work, typically the tissue is subjected to a low frequency (100–1000 Hz), low amplitude (tens of μm) harmonic excitation, and several images (4–8) of the displacement field at different times are recorded. While MR is a more expensive and slower imaging method than ultrasound, it has a higher sensitivity and resolution than ultrasound (Dutt *et al* 2000) and is able to access deeper regions, such as the brain (McCracken *et al* 2005). It is also possible to measure all three components of the displacement field by repeating the experiment with the

motion-sensitizing gradient along each of the measurement directions, and the measurements can be made either on a plane or in a three-dimensional (3D) volume. In ultrasound, the axial component, and sometimes the lateral component (with much lower accuracy than the axial component), of the displacement field in a plane are measured.

In order to determine the elastic shear modulus from the measured mechanical response, it is necessary to solve a parameter identification problem, which is a type of inverse problem. For the case of a dynamic excitation, most of the inversion approaches presented in the literature make two key assumptions to reduce the equations of elasto-dynamics down to the Helmholtz equation, where the displacement components decouple; see, for example, Oliphant *et al* (2001), Bercoff *et al* (2003), Manduca *et al* (2003) and McLaughlin *et al* (2006). These assumptions are that the gradient of the hydrostatic stress (i.e. pressure) and shear modulus fields are negligible. These assumptions introduce a certain level of inaccuracy, which will be investigated here. The advantages of these methods are that they only require a single component of the displacement field in their reconstructions, and because they are applied locally, on small regions, they are fast. Recently, Sinkus *et al* (2005) proposed a method where the curl-operator is applied to the balance of linear momentum equation, and neglecting gradients in the Lamé parameters, this eliminates the term associated with the second Lamé parameter, i.e. the hydrostatic stress term. That approach, however, has the disadvantage of resulting in third-order spatial derivatives of the data, and still requires the locally constant assumption on the Lamé parameters. The usual argument made for neglecting the hydrostatic stress term (see, for example, Oliphant *et al* (2001)) is that this term is associated with the longitudinal (compression) wave, and this wave is very long compared to the shear wave. For a homogeneous medium, this is indeed true, and, in fact, under these circumstances, the analysis in Sinkus *et al* (2005) is correct and demonstrates that these terms can be neglected. However, in the problem at hand, the media of interest are not homogeneous, and in fact, the goal is to find the spatial variations in the elastic properties. In this work, we demonstrate that the gradients in the hydrostatic stress term are not, in general, negligible for heterogeneous media with properties similar to that of soft tissue.

By using the finite element method the complete equations of elasto-dynamics can be considered. Van Houten *et al* (1999, 2000, 2001, 2003) present a finite element based method for solving the elastography problem with displacement data resulting from a time-harmonic excitation measured using MR. In that work, the inverse problem is posed as an optimization problem to find the elastic moduli that, when used in the governing equations on the domain of interest with appropriate boundary conditions, minimizes, in a least-squares sense, the difference between the computed and measured displacements. This problem is solved in an iterative fashion where the latest update of the elastic moduli are used in the forward solution of the governing equations to solve for the displacements; then the elastic moduli are updated using a Newton–Raphson step. This is repeated until convergence, which is reported to be typically about 30 iterations (Doyley *et al* 2003). The disadvantages of this algorithm are (1) it requires significant computational resources and is relatively slow because it is iterative and requires a full forward solution of the governing equations on the domain of interest in each iteration, and (2) it requires boundary conditions for the forward solution step, which presumably are the measured displacements, and thus, over-weights the boundary measurements (treats them as exact), while all the other measured displacements are matched only in a least-squares sense. It should be noted that Romano *et al* (2000) also present a novel finite element based technique where, by integrating the variational statement of the governing equations by parts twice, all derivatives on the displacement field are eliminated, and then, through appropriate choice of weighting functions, the unknown traction boundary conditions are eliminated from the equations. However, in integrating by parts the second time, they

neglect the gradients in the elastic moduli, and ultimately, they also neglect the gradients in the hydrostatic stress field. Thus, the same assumptions are used that reduce the equations of elasto-dynamics down to the Helmholtz equation.

In this paper, we present a finite element based, direct inversion method for solving the dynamic elastography problem assuming time harmonic motion. The current analysis is limited to linear, isotropic, elastic behaviour for the tissue. While tissue typically exhibits anisotropic and viscoelastic behaviour, this is presented as a first step and for comparison with other algorithms with similar limitations. Details about the reasonableness of these simplifications are explained very well by Ophir *et al* (1999). The algorithm solves for the shear modulus and hydrostatic stress distribution which minimize the residual of the equations of motion for prescribed displacements. The resulting equations are linear, so they can be solved directly, without iterations. In addition, the algorithm is designed so that no boundary conditions are required, and the displacement data are equally weighted. Furthermore, since the displacements are measured throughout the domain, not just on the boundary, the equations can be solved on sub-domains allowing for smaller scale, faster computations that are also readily parallelizeable. The main disadvantage of the direct inversion algorithm presented is that the measured displacement data need to be differentiated. In this work, a simple filter is used to smooth the potentially noisy displacement data and project it onto a volume preserving space prior to applying the inverse algorithm. We also present one example where a method designed, based on statistical analysis (Anderssen and Hegland 1999), for differentiating noisy data is used. Another disadvantage, as compared to the methods that solve the approximating Helmholtz equation, is that all three components of the displacement field are required as well as their gradients. In practice, this means that at least two components must be measured on two adjacent planes so that the gradients may be computed, and the third component may be reconstructed using the fact that the deformation is approximately volume preserving. A simple case involving a cylindrical inclusion is presented to examine the effects of contrast ratio and inclusion size on the data, to characterize the computational model error in terms of discretization and to investigate the effect of noise on the reconstruction solution. A more complicated case with three inclusions of varying size and contrast ratio is also considered. Finally, initial results from MR measured data in a phantom are presented.

2. Methods

2.1. Governing equations and problem definition

We first present the governing equations assuming linear elastic, time harmonic tissue motion. Let the tissue region of interest be defined as Ω, and the time harmonic motion be defined by the displacement field, $u(x)$, which depends on position $x \in \Omega$ for any given time. The usual forward problem is to find the displacement, $u(x)$, and hydrostatic stress, $p(x)$, fields that satisfy the following system, which is expressed in indicial notation (see, for example, Malvern (1969)),

$$[\mu(u_{i,j} + u_{j,i})]_{,j} + p_{,i} = -\rho\omega^2 u_i \quad \text{in } \Omega \tag{1}$$

$$p = \lambda u_{k,k} \quad \text{in } \Omega \tag{2}$$

$$u_i = \hat{u}_i \quad \text{on } \partial\Omega_{1i} \tag{3}$$

$$[\mu(u_{i,j} + u_{j,i}) + p\delta_{ij}]n_j = \hat{T}_i \quad \text{on } \partial\Omega_{2i} \tag{4}$$

where $\mu(x)$ is the shear modulus, which depends on position, ρ is the density, ω is the angular frequency of excitation and $\lambda(x)$ is a Lamé parameter. In addition, Roman subscripts indicate rectangular Cartesian components, and repeated indices imply summation. We also

introduce the usual shorthand notation $_{,j} \equiv \frac{\partial}{\partial x_j}$. Equations (1) and (2) together are the balance of linear momentum. It should be noted that for soft tissue the Lamé parameter, λ, which is associated with the elastic resistance to volume change, is about six orders of magnitude higher than the shear modulus, μ, which characterizes the tissue's elastic resistance to shape change. A typical value for λ is 2.3 GPa, while μ is of the order of kPa; thus $\lambda(\boldsymbol{x}) \gg \mu(\boldsymbol{x})$. For this reason, tissue is frequently referred to as nearly or relatively incompressible. In the case of nearly incompressible elastic behaviour, the elastic relations should be expressed in a mixed formulation, as given in equations (1) and (2) where the hydrostatic stress, p, is introduced as an additional variable for stability purposes when solving (Brezzi and Fortin 1991). Furthermore, it should also be mentioned that, in comparison to μ, λ and ρ do not vary much in soft tissue (Sarvazyan *et al* 1998). This is because λ and ρ are associated with the resistance to volume change and the density, respectively, and these properties, for soft tissue, are close to that of water because soft tissue is 70–80% water. For this reason, in this work the density, ρ, is treated as constant and known. Equations (3) and (4) are boundary conditions on the displacements and tractions. Equations (1) and (2), together with boundary conditions (3) and (4), yield a boundary value problem which can be solved for the displacement and hydrostatic stress fields if $\mu(\boldsymbol{x})$, $\lambda(\boldsymbol{x})$, ρ, ω, $\hat{u}_i$ and $\hat{T}_i$ are known. Finally, for completeness, either type of boundary condition must be specified at each location on the boundary in each direction without overlap, i.e. $\partial\Omega_{1i} \cup \partial\Omega_{2i} = \partial\Omega$ and $\partial\Omega_{1i} \cap \partial\Omega_{2i} = \emptyset$.

The problem of interest considered here is to find the shear modulus $\mu(\boldsymbol{x})$ that best satisfies equation (1), where the density ρ and the angular frequency ω are assumed known, given some measured displacement field at discrete locations in Ω for a given time,

$$u_i(\boldsymbol{x}_r) \approx u_i^m\left(\boldsymbol{x}_r^m\right) p = 1, \qquad N_m \boldsymbol{x}_r^m \in \Omega \tag{5}$$

where the superscript m indicates a quantity associated with a measurement, which is approximate due to normal experimental errors (e.g. noise) and N_m is the number of positions in space where measurements are taken. This is referred to as an inverse problem because what is normally part of the solution, the displacement field at discrete locations, is specified, and a coefficient in the governing equation $\mu(\boldsymbol{x})$ is the sought unknown. Specifically, this is an inverse problem of parameter identification. Furthermore, it should be noted that equation (2) cannot be used directly because, in soft tissue, due to the nearly incompressible behaviour, $u_{k,k}$ is a very small number multiplied by the very large number λ. Thus, small errors in the data lead to very large errors in p. So the hydrostatic stress, $p(\boldsymbol{x})$, must also be treated as an unknown, where it is whatever it needs to be to best satisfy balance of linear momentum (1).

There are several approaches to solving this inverse problem. A common approach is to assume that $u_{k,k} = 0$, i.e. the displacement field is exactly divergence free, which implies the deformation is volume preserving and there is no hydrostatic stress (2). With this assumption, (1) reduces to $\mu_{,j}(u_{i,j} + u_{j,i}) + \mu u_{i,jj} = -\rho\omega^2 u_i$. Furthermore, if the gradient of the shear modulus is also neglected, this equation reduces finally to $\mu u_{i,jj} = -\rho\omega^2 u_i$, a Helmholtz equation for each of the displacement components. As mentioned in the introduction, both of these assumptions are commonly made in solution approaches in the literature, but will not be made here, and the validity of neglecting the hydrostatic stress term will be examined.

Considering again the full equation in (1), we can see that there are two unknown fields, the shear modulus, μ, and hydrostatic stress, p, and three equations, if all the components of the displacement field and its derivatives are known. Thus, there appear to be sufficient equations to obtain a solution, although this is not a uniqueness proof. Uniqueness has been shown for the transient, dynamic case where the two Lamè parameters are sought (McLaughlin and Yoon

2004), which is a closely related problem. However, the hydrostatic stress in (1) appears as a gradient; so given only displacements, p can only be determined to within a constant.

Based on this observation, one might try to put the data, or some filtered form of the data, directly into equation (1), and solve directly for μ and p. However, this requires differentiating the data twice, which may lead to large errors in the solution and poor spatial resolution. Using a finite element weak form, we decrease the order of derivatives in the differential equations by one. Furthermore, the finite element method converts the problem into a finite dimensional subspace, which is a natural subspace in which to work given the spatially discrete data.

2.2. Finite element approximation

Let the displacement field $u(x)$, hydrostatic stress $p(x)$ and shear modulus $\mu(x)$ be approximated in terms of typical finite element basis functions such that

$$u_i(x) \approx u_i^h(x) = \bar{u}_{i\alpha}\psi_\alpha(x), \qquad \alpha = 1, N_u \tag{6a}$$

$$p(x) \approx p^h(x) = \bar{p}_\gamma \tilde{\psi}_\gamma(x), \qquad \gamma = 1, N_p \tag{6b}$$

$$\mu(x) \approx \mu^h(x) = \bar{\mu}_\eta \check{\psi}_\eta(x), \qquad \eta = 1, N_\mu \tag{6c}$$

where the superscript h indicates a finite dimensional approximation and ψ_α, $\tilde{\psi}_\gamma$ and $\check{\psi}_\eta$ are finite element basis functions for the displacement, hydrostatic stress and shear modulus fields, respectively. Greek subscripts refer to finite element shape function numbers. Overbar ($\bar{}$) denotes coefficients of interpolating functions, which, for standard finite element basis functions, coincide with the interpolated values at the finite element nodes.

Taking the weak form of equation (1) and substituting in the finite dimensional approximations yields

$$\int_\Omega \left[\mu^h \left(u_{i,j}^h + u_{j,i}^h \right) + p^h \delta_{ij} \right] w_{i,j}^h \, \mathrm{d}V = \int_\Omega \rho \omega^2 u_i^h w_i^h \, \mathrm{d}V + \int_{\partial\Omega_2 i} \hat{T}_i w_i^h \, \mathrm{d}A \tag{7}$$

and likewise, equation (2) takes on the form

$$\int_\Omega \left(u_{k,k}^h - \frac{p^h}{\lambda} \right) q^h \, \mathrm{d}V = 0 \tag{8}$$

where w^h and q^h are arbitrary, discrete trial functions defined in terms of the same finite element interpolating functions as u^h and p^h, respectively. Equations (7) and (8) represent the usual finite element formulation for solving the forward problem for the interpolated displacement and hydrostatic stress fields, $u^h(x)$ and $p^h(x)$, on the domain, which is now reduced to solving for the coefficients of the interpolating functions, $\bar{u}_{i\alpha}$ and $\bar{p}_\gamma$, when the shear modulus μ^h and boundary conditions (3) and (4) are given. It should be noted that Galerkin methods applied to nearly incompressible material behaviour, as is the case for soft tissue, in the setting of a mixed finite element method, must fulfil the Ladyzenskaya–Babuska–Brezzi (LBB) condition to achieve unique solvability, convergence and robustness (Brezzi and Fortin 1991). This places restrictions on the choice of the solution space. Specifically, the interpolation functions ψ_α and $\tilde{\psi}_\gamma$ should satisfy the LBB condition to avoid large errors or oscillations in the forward solution. In general, the interpolation functions for the hydrostatic stress are of lower order than that for the displacement field.

However, in this case, we are interested in solving for the interpolated shear modulus field μ^h when the displacement field on the domain is given approximately from measurements at discrete locations. The approach to solving this inverse problem is described next.

2.3. Inverse problem solution approach

As discussed in section 1, a direct inversion approach is used in this work to reconstruct the shear modulus field. This approach is taken because it does not require iterations and can be applied on any sub-domain of the region of interest allowing for fast computation of the solution. This approach centres on solving equation (7) for the shear modulus and hydrostatic stress fields, μ^h and p^h, directly. However, in solving the inverse problem using this approach, several important issues arise. First, the boundary tractions, $\hat{T}$, appearing on the right-hand side of equation (7) are not known. These tractions are the stresses that the material surrounding the region of interest applies to the interface, the boundary of Ω, $\partial\Omega$. Second, the displacement data are only known approximately, and derivatives of the displacement data appear in our governing equations. Directly differentiating noisy data will cause large errors in the solution. Third, the displacement data are only known at discrete locations, which may not be sufficiently, finely spaced to satisfy mesh convergence in the forward solution. Thus, if the same discretization is used in the finite element model on which the inversion is based, the error in the model may be significant. We will address each of these issues.

Considering again equation (7), substituting in the finite element interpolants for the shear modulus and hydrostatic stress from (6) as well as for the weighting function w^h, and considering the arbitrariness of the weighting function, the following system of equations results,

$$\int_\Omega \left[\left\{ \bar{\mu}_\eta \check{\psi}_\eta \left(u_{i,j}^h + u_{j,i}^h \right) + \bar{p}_\gamma \tilde{\psi}_\gamma \delta_{ij} \right\} \psi_{\beta,j} \right] dV = \int_\Omega \rho\omega^2 u_i^h \psi_\beta \, dV + \int_{\partial\Omega} \hat{T}_i \psi_\beta \, dA, \tag{9}$$

which is to be solved for the coefficients of the interpolants, $\bar{\mu}_\eta$ and $\bar{p}_\gamma$. This results in a system of equations of the form

$$[\mathbf{K}]\{\boldsymbol{\mu}\} + [\mathbf{G}]\{\mathbf{p}\} = \{\mathbf{f}\} \tag{10}$$

where $\{\boldsymbol{\mu}\}$ and $\{\mathbf{p}\}$ represent the assembled coefficients of the interpolants for the shear modulus $\bar{\mu}_\eta$ and hydrostatic stress $\bar{p}_\gamma$. Matrices $[\mathbf{K}]$, $[\mathbf{G}]$ and $\{\mathbf{f}\}$ are coefficient and force matrices which are assembled from the following element matrices:

$$K_{i\beta\eta}^e = \int_{\Omega^e} \check{\psi}_\eta \left(u_{i,j}^h + u_{j,i}^h \right) \psi_{\beta,j} \, dV \tag{11}$$

$$G_{i\beta\gamma}^e = \int_{\Omega^e} \tilde{\psi}_\gamma \psi_{\beta,i} \, dV \tag{12}$$

$$f_{i\beta}^e = \int_{\Omega^e} \rho\omega^2 u_i^h \psi_\beta \, dV + \int_{\partial\Omega^e} \hat{T}_i \psi_\beta \, dA \tag{13}$$

where $\Omega^e \subset \Omega$ is a finite element and $\partial\Omega^e \subset \partial\Omega$ is any part of the element boundary that also lies on the region of interest boundary. This is a system of $n \times N_u$ equations, where n is 2 for two-dimensional (2D) (plane strain) and 3 for 3D displacement information, with $N_\mu + N_p$ unknowns. As mentioned in the previous section, the interpolation order for the displacement field must be larger than that for the hydrostatic stress for stability; thus $N_u > N_p$. Furthermore, the interpolated shear modulus would typically be the same or lower order than the displacement interpolation, $N_u \geqslant N_\mu$. Thus, this system has more equations than unknowns allowing for a best fit solution to be sought. Note that since the system is being solved now for the shear modulus and hydrostatic stress fields, knowledge of boundary displacements cannot be used to eliminate the need for the traction boundary condition in equation (9). Thus, in this case, the traction is required on the entire boundary, i.e. $\partial\Omega$ replaces $\partial\Omega_{2i}$ in the weak form of the governing equation. From a physical point-of-view,
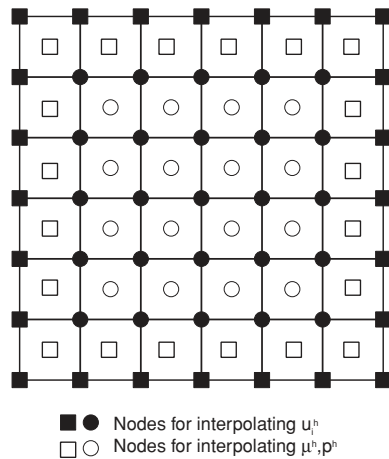
■ ● Nodes for interpolating u^h
□ ○ Nodes for interpolating μ^h, p^h

Figure 1. Schematic view of finite element model. Nodal interpolants for $\boldsymbol{u}^h$, $\boldsymbol{w}^h$ are bilinear, continuous and for μ^h and p^h are constant, discontinuous.

the left-hand side of equation (9) represents the internal force, the first term on the right-hand side represents the inertial force, and the second term on the right-hand side represents the externally applied force. These forces must balance.

The first difficulty that must be addressed is the fact that the tractions the surrounding material exerts on $\partial\Omega$, in the second term on the right-hand side of equation (9), are not known. An easy solution is to throw out the equations associated with these unknown boundary tractions. However, this may result in insufficient equations for unique solution. Consider the simple example illustrated in figure 1. Suppose the displacement field is interpolated with continuous, bilinear functions and the hydrostatic stress and shear modulus are interpolated with discontinuous, constant functions. Then the nodes associated with the equations are denoted ■ and ●, and the nodes associated with the unknown shear modulus and hydrostatic stress are denoted □ and ○. From the diagram, we see that there are 72 unknowns. If we discard the equations associated with the unknown traction boundary conditions, i.e. those associated with nodes marked ■, then we have, for the 2D case (i.e. plane strain case), 50 equations, since every node marked with ● has two equations associated with it, one for each degree of freedom. In this case, the system is under-determined. On the other hand, if this were a 3D case, i.e. all three components of the displacement and its gradients were known and the strain was non-planar on this 2D domain, then we would have 75 equations, and the system would be over-determined. For the under-determined case, we assume that the shear modulus μ^h and hydrostatic stress p^h on the elements on the boundary, marked with □, are identical with those of the nearest neighbouring element, marked with ○. With this assumption, the number of unknowns is reduced to 32, and the system becomes over-determined, for which a least-squares fit could be used for finding the best solution. Adopting a least-squares fit to the solution, we obtain the system of equations to be solved for μ and $\mathbf{p}$:

$$\begin{bmatrix} \mathbf{K}^T\mathbf{K} & \mathbf{K}^T\mathbf{G} \\ \mathbf{G}^T\mathbf{K} & \mathbf{G}^T\mathbf{G} \end{bmatrix} \begin{bmatrix} \boldsymbol{\mu} \\ \mathbf{p} \end{bmatrix} = \begin{bmatrix} \mathbf{K}^T\mathbf{f} \\ \mathbf{G}^T\mathbf{f} \end{bmatrix}. \tag{14}$$

The second difficulty, and one of the most serious drawbacks of the direct inversion method, is that it is sensitive to noise in the measured displacements due to the spatial derivative term in (11). Thus, instead of using the measured displacement data directly in

the direct inversion method described above, we must use filtered displacement data that satisfy certain conditions. In particular, we find a displacement field that is smooth, volume preserving, and close to the measured displacements that lies in our finite dimensional space defined by the finite element interpolation (6a). To enforce smoothness, we require $\nabla \boldsymbol{u}^h$ to be finite. To enforce volume preserving deformation, which satisfies the nearly incompressible behaviour of soft tissue, we drive the divergence of the displacement field, $\nabla \cdot \boldsymbol{u}^h$, to near zero. To accomplish these objectives, we find the displacement field that lies in the finite dimensional space defined in terms of our finite element basis functions (6a) and that minimizes

$$F(\boldsymbol{u}^h) = \frac{1}{2}\alpha_1 \int_\Omega \left(\nabla \cdot \boldsymbol{u}^h\right)^2 \mathrm{d}V + \frac{1}{2}\alpha_2 \int_\Omega \|\nabla \boldsymbol{u}^h\|^2 \mathrm{d}V + \frac{1}{2}\alpha_3 \int_\Omega \|\boldsymbol{u}^h - \boldsymbol{u}^m\|^2 \mathrm{d}V, \qquad (15)$$

where α_1, α_2 and α_3 are weighting coefficients and $\|\cdot\|$ indicates L^2 norm. The first term enforces incompressibility, the second term enforces smoothness and the third term forces the filtered displacement data to be close to the measured data. The constraint on the displacement gradient is weak relative to the other constraints, and the small divergence is the strongest constraint; thus $\alpha_2 \ll \alpha_3 \ll \alpha_1$. The above equation is expressed in terms of the finite element basis functions, where the finite element nodal points match the measurement locations. An advantage of this smoothing approach is that it reduces the degrees of freedom of data required. Specifically, the divergence free constraint allows one unknown component of the displacement field to be obtained. Thus, for 2D displacement fields, only one displacement component is needed, and for 3D displacement fields, only two components are needed on adjacent planes.

Using this optimization smoothing approach, we obtain a smoothed displacement field and then spatially differentiate it using finite element shape function to obtain strain values needed in (11). From (6a), the differentiation is expressed as the equation

$$u^h_{i,j} = \bar{u}_{i\alpha} \psi_{\alpha,j} \qquad (16)$$

where $\bar{u}_{i\alpha}$ is a nodal value of u_i. We treat these filtered data as exact and fit them to the governing equation.

The third difficulty is associated with the model error that may arise if the grid on which the data are taken is also used as the finite element grid, i.e. nodal points, and that grid is not sufficiently fine for an accurate forward solution. This issue will be addressed in the next section through numerical experiments.

3. Numerical experiments

3.1. Cylindrical inclusion

First, a simple 2D, plane strain case with a cylindrical inclusion is used to investigate the effect of model discretization error, the sensitivity of the resulting displacement field to the inclusion size and contrast ratio, and effect of data error on the reconstructed shear modulus field. Figure 2 shows a schematic. A 50 mm square domain is subjected to a 150 Hz horizontal excitation with 1 mm amplitude on the top surface, and the bottom surface is fully constrained. The sides are traction free. The radius of the inclusion is denoted r. The shear modulus of the background material is taken to be $\mu = 36$ kPa and the other Lamé parameter is taken to be $\lambda = 2.3$ GPa, which together coincide with a Poisson's ratio of 0.499 992 (0.5 is exactly incompressible). The density ρ is taken to be 1000 kg m^{-3}, which is typical of soft tissue. The displacement is assumed to be 'measured' on the 40 mm square on the interior of the domain, demarcated with the dashed lined.
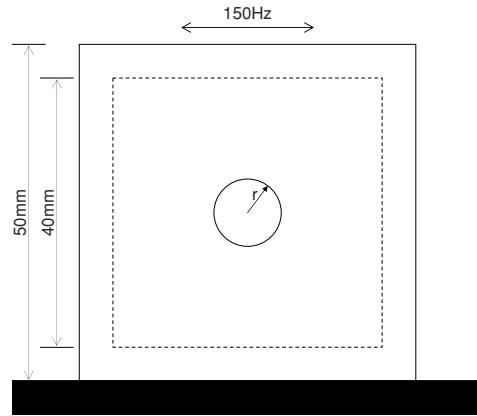
Figure 2. Schematic showing geometry and boundary conditions for the case of a cylindrical inclusion. Displacements only within the dashed line are collected on a regular grid and used as the data.

To investigate the model discretization error, we consider the case with $r = 0$, i.e. with no inclusion, which will also be used as a reference to the cases with cylindrical inclusions to investigate the sensitivity of the data to the inclusion. There are two reasons we are interested in the discretization error. First, the displacement measurement is given with predefined spatial resolution which is limited by the imaging modality. This provides a natural discretization for the finite element model on which the inversion approach for reconstructing the shear modulus field is based. The accuracy of this model significantly affects the accuracy of the reconstruction. Second, to test our inverse finite element algorithm, we first use synthetic data generated by a forward finite element algorithm, and we want to ensure that the synthetic data are accurate and are from a different model, i.e. solved on a different mesh, than that used in the inverse algorithm. To investigate the discretization error, we solve the forward problem for the displacement field on a sequence of meshes with different mesh sizes h, where h is the size of the edge of our square finite elements. Continuous, bi-linear, quadrilateral elements (Q1) are used for interpolating the displacement field, and discontinuous, constant elements (Q0) are used for interpolating the hydrostatic stress and shear modulus fields. While this element does not strictly satisfy the Babuska–Brezzi condition, it has been proven to give optimal convergence when used appropriately (Hughes 1987). Figure 3 shows the standard deviation between the calculated displacements at the nodes for a given element size and reference displacements at the same locations. The standard deviation is calculated by

$$\sigma^{\mathrm{mesh}} = \sqrt{\frac{\sum \|\boldsymbol{u}^c - \boldsymbol{u}^r\|^2}{N}} \tag{17}$$

where the superscripts c and r indicate calculated and reference displacements, and where the reference displacement field is taken from the solution on the finest grid. From figure 3, we see that the model discretization error for a mesh with a 1 mm grid spacing is approximately 0.01 mm, or about 1% of the excitation amplitude, and for a 0.5 mm grid spacing is about 0.003 mm or about 0.3% of the excitation amplitude. This is the range of typical experimental spatial resolution, and provides an estimate of the error in the model that will be used in the inversion algorithms.

Next, we investigate the sensitivity of the displacement field with respect to the inclusion size and shear modulus contrast ratio. We solve for the displacement field in each case using
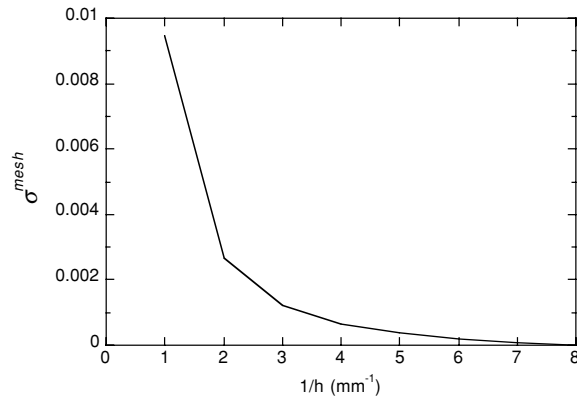
Figure 3. Displacement solution converges as mesh density increases; h is the element length.
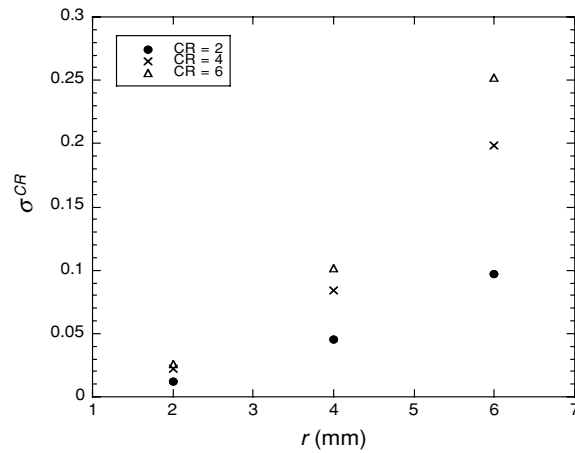

Figure 4. Standard deviation in the displacement field from the reference displacement field (with no inclusion) for different inclusion sizes and CRs.

the fine mesh, with $h = 0.125$ mm, to ensure an accurate solution. The shear modulus contrast ratio (CR) is defined as the ratio of the shear modulus of the inclusion to that of the background. The background shear modulus remains 36 kPa. Three CRs are considered, 2, 4 and 6, resulting in inclusion shear modulus values of 72 kPa, 144 kPa and 216 kPa, respectively. For each CR, three inclusion sizes are considered, $r = 2$, 4 and 6 mm. The standard deviation between the displacement field with the inclusion and the displacement field with no inclusion is computed for each case, denoted as σ^{CR} and defined similarly to σ^{mesh} in (17). The purpose of this study is to provide an indication of the detectibility of the inclusion. If the perturbation of the displacement due to the inclusion is less than the error from modelling or measurement, then it becomes difficult to detect the inclusion. The results are shown in figure 4. From this figure we see, for example, that an inclusion with a 6 mm radius and a CR of 2 has approximately the same detectability as an inclusion with a 4 mm radius and a CR of 6. From further investigation, we find that the relationship between the perturbation in the displacement field due to a stiff inclusion, σ^{CR}, and the CR and inclusion
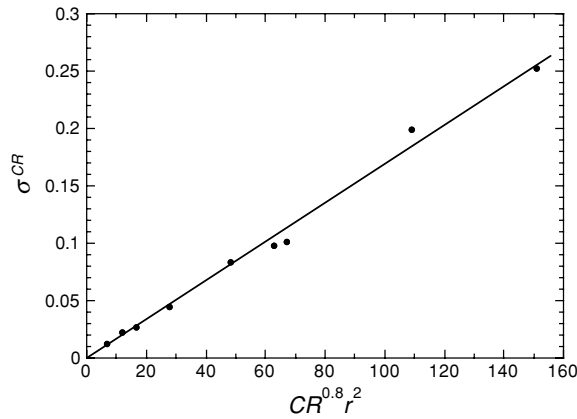
Figure 5. Curve fit (solid line) relating the standard deviation in the displacement field from the reference displacement field (with no inclusion) to the inclusion radius and CR. Solid circles are data points from numerical experiments.

radius together are approximately related by the following

$$\sigma^{\mathrm{CR}} \propto \mathrm{CR}^{0.8} r^2. \tag{18}$$

A plot of this relationship together with the data is shown in figure 5. This indicates that, at least for this 2D case, the detectability is roughly proportional to the area of the inclusion. In future work, we plan to investigate whether detectability scales with the inclusion volume for the more general 3D case.

To investigate the effect of the error in the data on the reconstruction, we solve for the shear modulus field using the calculated data, but on a much coarser mesh than is used to generate the synthetic data, with Gaussian random error added to the data. As mentioned before, we solve the reconstruction problem on a coarser mesh because this represents a typical grid on which data may be supplied. Furthermore, it is important to test inversion algorithms using data generated from a different model than that used in the inversion. To generate the synthetic data, we start with accurate results for the displacement field solved on a fine mesh ($h = 0.125$ mm), downsample to a coarse mesh ($h = 1$ mm), and then add different levels of Gaussian random error. Specifically, the following equation is used to generate the synthetic data:

$$u_i^m(\boldsymbol{x}) = u_i^c(\boldsymbol{x}) + u_i^{\mathrm{avg}}\varepsilon_i(\boldsymbol{x}) \tag{19}$$

where $\varepsilon_i(\boldsymbol{x})$ is a random number for each position, $\boldsymbol{x}$, on the coarse grid along each coordinate direction, i, and where the superscripts m, c and avg indicate the synthetic data value, the accurate computed value and the average value, respectively. The average value along each coordinate direction, u_i^{avg}, is the mean average of the displacement values defined as

$$u_i^{\mathrm{avg}} = \frac{1}{\Omega} \int_{\Omega} \left| u_i^c(\boldsymbol{x}) \right| \mathrm{d}V. \tag{20}$$

A total of eight cases are considered. In each case, CR $= 6$. Two inclusion sizes are considered, $r = 2$ mm and $r = 6$ mm. For each inclusion size, four different levels of error are considered, 0, 1, 3 and 5%, where these values represent the standard deviations of the Gaussian random numbers $\varepsilon_i(\boldsymbol{x})$.

To solve the inverse problem, the approach described in section 2.3 is followed. First, the synthetic measured data (only for the cases with error added to the data) are smoothed
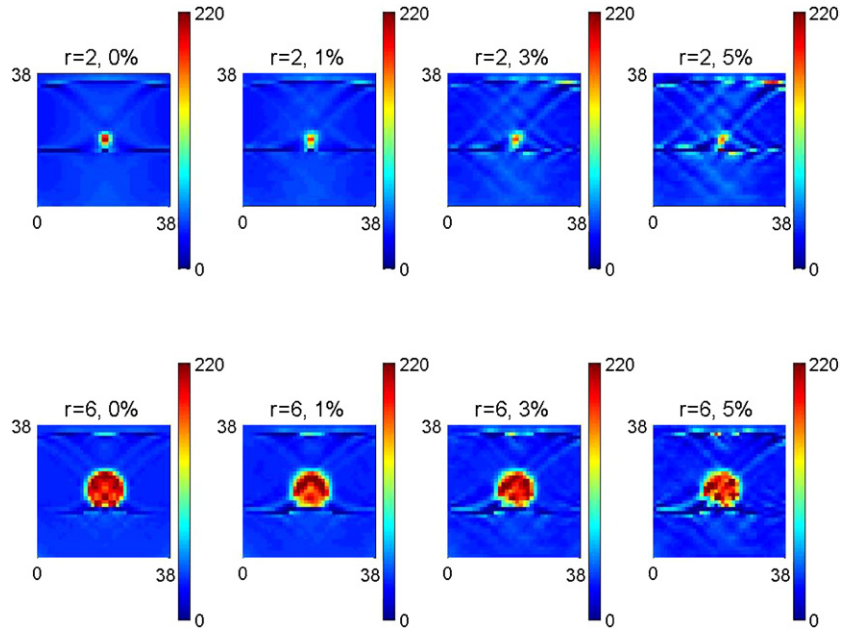
Figure 6. Reconstructed images of shear modulus for different levels of added error and inclusion sizes. The size (radius) in mm and the standard deviation of the added Gaussian random noise is indicated on top of each image. All dimensions of images are in mm and the unit of the colourbar is kPa.

by minimizing the function in (15). In all cases, $\alpha_1 = 1000$, $\alpha_2 = 0.01$, and $\alpha_3 = 10$. As mentioned before, since α_1 enforces the divergence to be small, it is taken to be the largest parameter, and since α_3 enforces the smoothed displacements to be near the 'measured' displacement, it is also taken to be large, but not as large as α_1. Furthermore, since α_2 applies a penalty on the gradient of the displacement field to smooth the data, it is taken to be a relatively small number so as to smooth the data without altering it too much. The precise choice of the weighting parameters was found not to have a strong effect on the solution, and the choice used here may not be the optimal choice. Then the system in (14) is formed and solved.

Figure 6 shows the reconstructions for each case, and table 1 provides more quantitative results. First, considering figure 6, in all cases, the inclusion is well detected; however, the edges are smoothed some and the magnitude of the shear modulus in the inclusion is slightly under-predicted. This is due to the smoothing of the displacement field and the coarseness of the discretization. Artefacts can also be seen running diagonally through the domains, becoming more pronounced at higher levels of error. This is due both to the coarseness of the mesh and to instabilities in the solution for the hydrostatic stress. This will be discussed further in the next section with regard to the multiple inclusion case. Table 1 lists the per cent error in the 'measured' displacement data, E_{u^m}, in the smoothed displacement displacement data used in the inversion algorithm, E_{u^h}, and in the reconstructed shear modulus, E_μ. In addition, it also lists the average reconstructed shear modulus in the inclusion, $\mu_{\text{avg}}^{\text{inc}}$, for each case. The per cent error in the 'measured' displacement data is described in (19) and (20). E_{u^h} is defined as

$$E_{u^h} = \frac{\Delta u}{\bar{u}} \tag{21}$$

Table 1. Added Gaussian random error, E_{u^m}, in the synthetic displacement data, average error in the smoothed displacement field, E_{u^h}, average error in the reconstructed shear modulus, E_μ, and average shear modulus in the inclusion, $\mu_{\text{avg}}^{\text{inc}}$ for cases with 2 mm and 6 mm inclusion radii.

	E_{u^h} (%)		E_μ (%)		$\mu_{\text{avg}}^{\text{inc}}$ (kPa)	
E_{u^m} (%)	$r = 2$ mm	$r = 6$ mm	$r = 2$ mm	$r = 6$ mm	$r = 2$ mm	$r = 6$ mm
0	0	0	21.91	27.53	179.6	191.2
1	0.49	0.61	26.42	31.55	153.7	184.4
3	1.20	1.17	31.07	36.15	142.3	182.1
5	1.95	1.82	49.05	45.27	144.0	164.0

where

$$\Delta u = \sqrt{\frac{1}{\Omega} \int_\Omega (\boldsymbol{u}^c - \boldsymbol{u}^h) \cdot (\boldsymbol{u}^c - \boldsymbol{u}^h) \, \mathrm{d}V} \tag{22}$$

$$\bar{u} = \sqrt{\frac{1}{\Omega} \int_\Omega \boldsymbol{u}^c \cdot \boldsymbol{u}^c \, \mathrm{d}V}. \tag{23}$$

E_μ is defined similarly for the error in the reconstructed shear modulus. From these results, we make the following observations. First, the data 'smoothing' reduces the error in the data used in the reconstruction substantially. Second, although the reconstructions in figure 6 appear pretty good, as far as detecting the inclusion, there is substantial error in the reconstructed shear modulus, even when no error is added to the data. This is largely attributed to the artefacts, which could be reduced with some post-processing, for example with a median filter. It should also be noted that the average error over the whole domain is actually higher for the larger inclusion due to these artefacts, although the modulus recovered in the inclusion is more accurate. These artefacts may also be reduced with some modification to the reconstruction algorithm as the solution for the hydrostatic stress field is ill-conditioned. Some added regularization on the hydrostatic stress would improve the condition of the system in equation (14). Third, the average reconstructed shear modulus in the inclusion is consistently below the specified value of 216 kPa, and becomes more under-predicted as the level of error increases in the data. This is due, in part, to the smoothing of the displacement data.

3.2. Multiple inclusions

The shear modulus reconstruction algorithm is now tested on a more complicated case involving multiple inclusions of different size, shape and contrast ratio. In this example, we investigate the effect of error and the effect of neglecting the gradient in the hydrostatic stress on the reconstruction. The geometry considered is similar to the prior example and is shown in figure 7. As in the prior example, a 50 mm square domain is subjected to a 150 Hz horizontal excitation with 1 mm amplitude on the top surface, while the bottom surface is fully constrained, and the sides are traction free. The background material has a shear modulus of $\mu = 36$ kPa. For all materials, the other Lamé parameter is taken to be $\lambda = 2.3$ GPa, and the density is taken to be 1000 kg m^{-3}. The CR of the shear moduli of the three inclusions are 2, 4 and 6, as shown, and the smallest inclusion has a radius of 2 mm. The displacement is assumed to be 'measured' on the interior 40 mm square region.

As in the prior example, a finite element model with a mesh size of $h = 0.125$ mm is used to generate the synthetic data, but only the data downsampled to a coarser mesh with
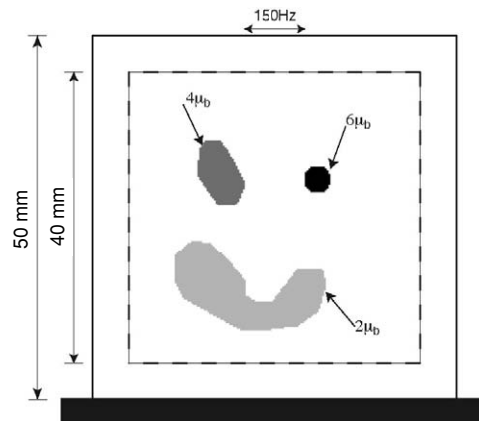
Figure 7. Schematic showing geometry and boundary conditions for the case with multiple inclusions.
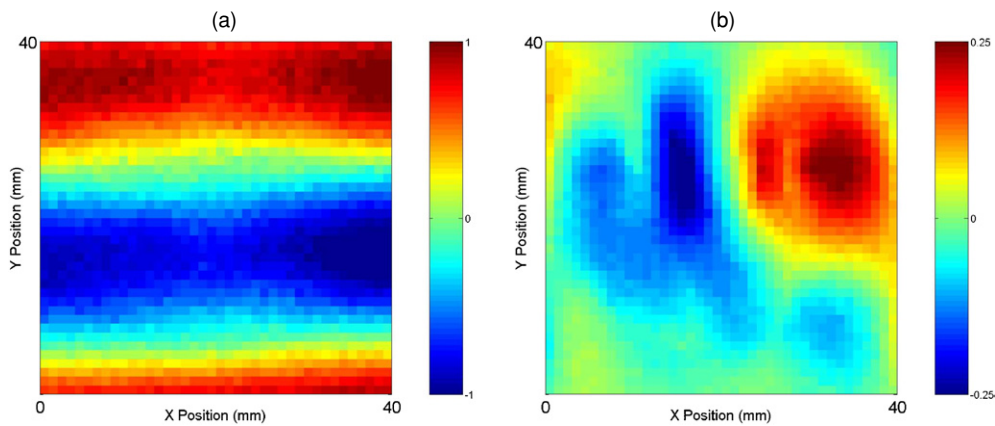

Figure 8. Displacement data (in mm) with 5% Gaussian random error used in the reconstruction: horizontal component (a) and vertical component (b).

$h = 1$ mm are used in the reconstruction to simulate a typical grid on which experimental data might be collected. Then Gaussian random error, with a standard deviation of 5% of the average displacement, is added in the same way as in the previous example using (19) and (20). The data with the error included are shown in figure 8. It is not obvious, from visual inspection of the displacement field, where the inclusions are. Finally, as in the prior example, the data are smoothed before the shear modulus reconstruction is performed by minimizing the function in (15). As in the previous example, the weighting parameters are taken to be $\alpha_1 = 1000$, $\alpha_2 = 0.01$ and $\alpha_3 = 10$.

Results for the shear modulus reconstruction are shown in figure 9. Figure 9(a) shows the reference shear modulus distribution and figures 9(b)–(d) show the reconstructions with no error in the data, with error and no smoothing of the data before reconstructing μ, and with error and smoothing before reconstructing μ, respectively. The case using the computed displacements without error and downsampled to the coarse mesh (figure 9(b)) shows the results including only the discretization error for the coarse mesh. All three inclusions are
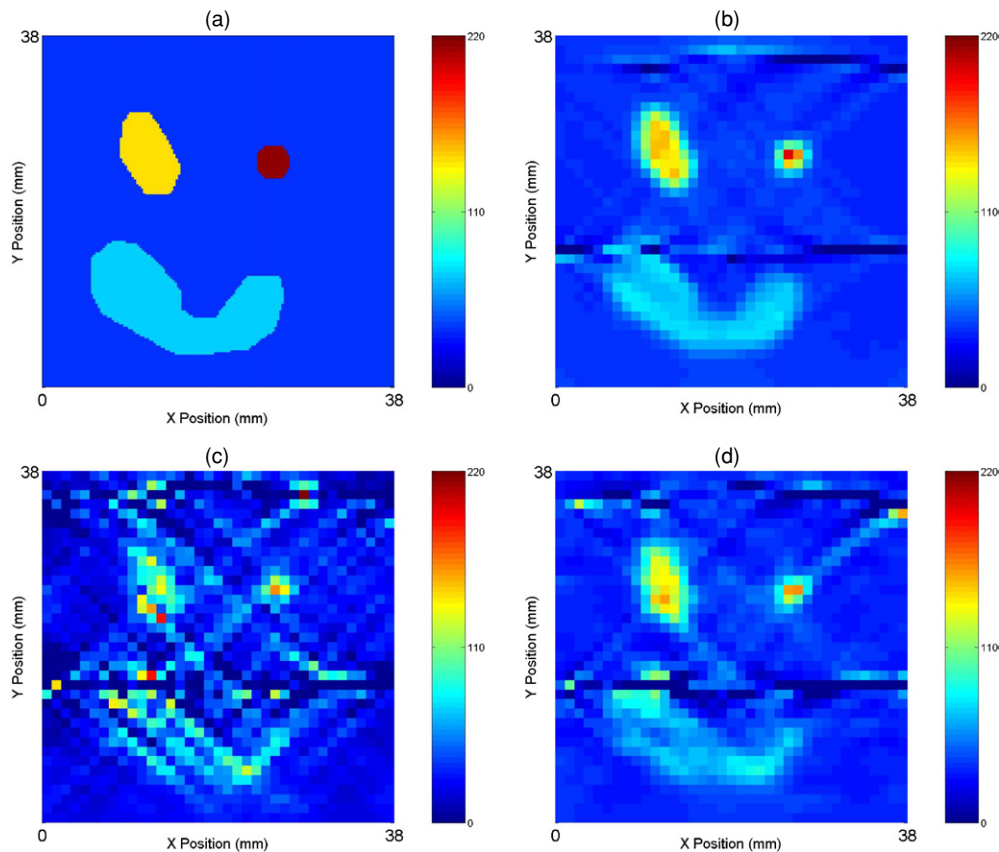
Figure 9. Results for shear modulus recovery (in kPa): (a) specified value, (b) recovery using exact finite element forward solution data (downsampled to inverse problem mesh), (c) recovery using data with 5% Gaussian random error added without smoothing the data and (d) recovery using data with 5% Gaussian random error added and smoothing the data before recovery.

well detected, not only in terms of the size and the location of the inclusions, but also in terms of the values of the shear moduli. However, the boundaries of the inclusions are not as sharp, and some artefacts are seen due to the discretization error. The case with the 'noisy data' used directly in the reconstruction without prior smoothing (c) generates a result that is dominated by artefacts and noise, making detection difficult. Finally, the case where the 'noisy data' is smoothed before reconstruction (d) generates a reconstruction where the inclusions are detected, but significant artefacts are also present. Interestingly, the artefacts appearing in the multiple inclusion case also run diagonally as in the case with a single inclusion. We will now investigate one of the primary sources of these artefacts, the ill-posedness in the reconstruction of the hydrostatic stress field.

As mentioned in the introduction, a key assumption frequently made in inversion algorithms for reconstructing the shear modulus is that the gradient in the hydrostatic stress field is negligible. The validity of this assumption is now considered, and the effect of the hydrostatic stress field on the reconstructed shear modulus is investigated. Figure 10(a) shows the reconstructed hydrostatic stress field from the inversion algorithm, which is reconstructed simultaneously with the shear modulus. Figure 10(b) shows the hydrostatic stress field
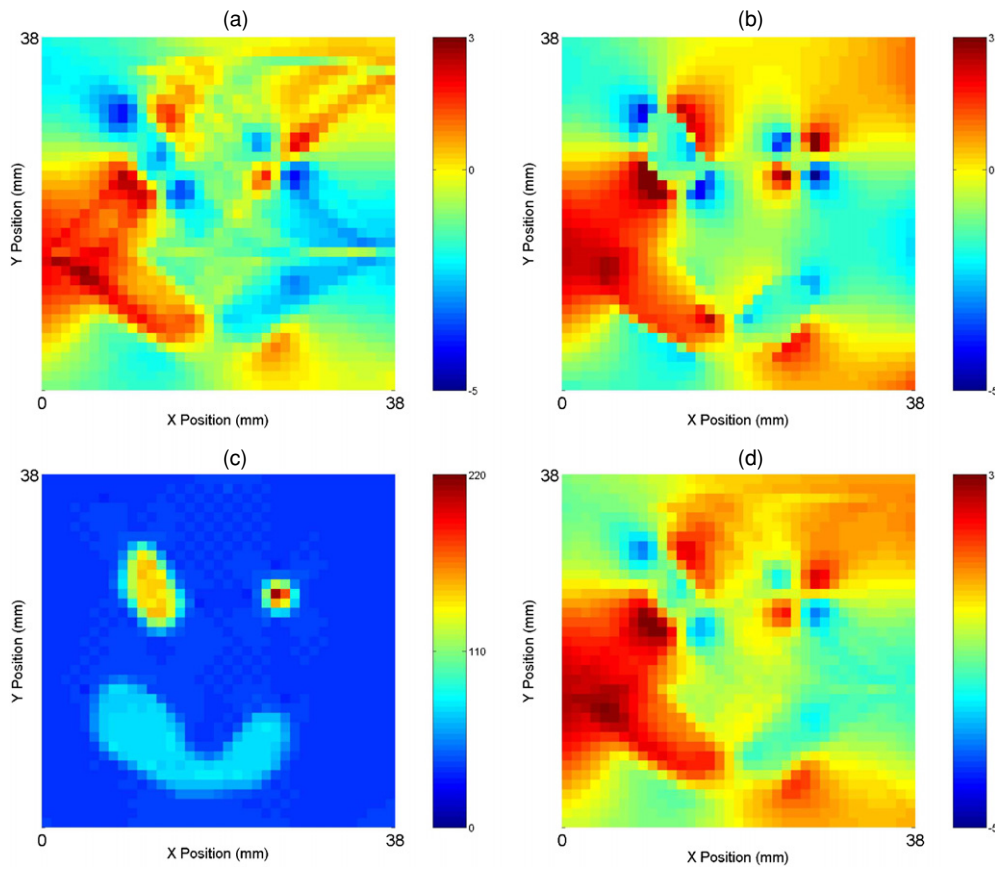
Figure 10. Hydrostatic stress distribution in region of interest (a) recovered in inverse problem solution and (b) from forward calculation (in kPa). (c) Shear modulus recovery (in kPa) with hydrostatic stress from forward solution. (d) Recovered hydrostatic stress distribution after smoothing.

calculated from the forward simulation. One can see in figure 10(a) that the hydrostatic stress field shows the same artefact pattern as the reconstructed shear modulus field. This is due to the ill-posedness of the hydrostatic stress recovery. To see the effect of the hydrostatic stress recovery, the hydrostatic stress field in figure 10(b) is used in (10) and then solved only for the shear modulus distribution. A good, quantitative reconstruction of the shear modulus distribution is obtained without any artefact in figure 10(c), indicating the importance of the hydrostatic stress recovery.

To see the effect of neglecting the hydrostatic stress gradient in the reconstruction, figure 11(a) shows the reconstruction of the shear modulus using the same inversion algorithm neglecting the hydrostatic stress term. Comparing this result with figures 9(a) and (b), showing (a) the prescribed shear modulus field, (b) that recovered together with the hydrostatic stress field, we observe that the reconstruction including the hydrostatic stress term is much better at capturing the actual values of the shear moduli, but contains artefacts. On the other hand, the reconstruction neglecting the hydrostatic stress field does not capture well the actual values of the shear moduli, and, in fact, consistently underpredicts the values, but the solution is
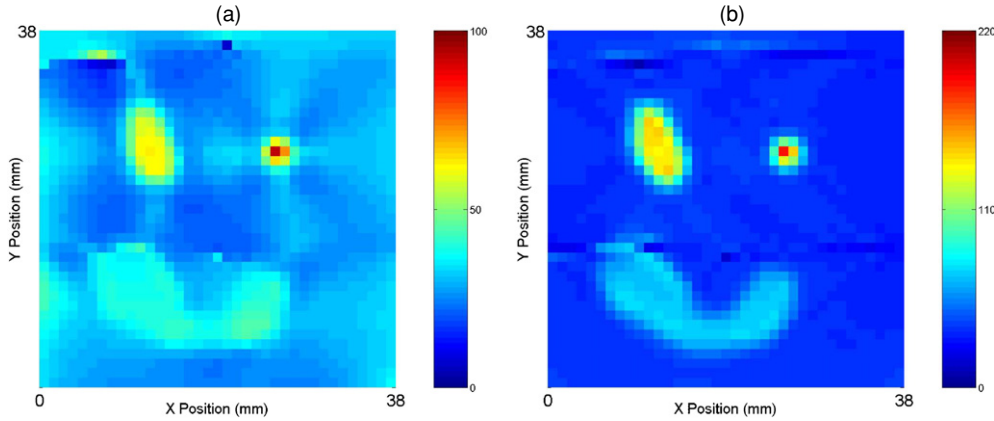
Figure 11. Shear modulus recovery (in kPa): (a) recovery neglecting hydrostatic stress term and (b) recovery with smoothing hydrostatic stress field.

smoother, with fewer artefacts. This further indicates that the hydrostatic stress term is the source of ill-posedness which leads to the instabilities in the solution that appear as artefacts in the reconstructions. From these observations, (a) we can conclude that the hydrostatic stress gradient is not, in general, negligible, and should be included in order to obtain accurate values of the shear modulus in the reconstruction (which may be important for diagnosis) and (b) we postulate that we can likely improve the algorithm by stabilizing the hydrostatic stress field. That will be presented in the next sections together with an example using experimental data on a tissue-mimicking phantom.

3.3. Stabilization of hydrostatic stress

A simple regularization approach is described to improve stability in the hydrostatic stress reconstruction and reduce artefacts in the reconstruction of the shear modulus field. It is not surprising that the hydrostatic stress recovery exhibits instabilities. First, the governing equation (1) is in terms of a gradient of the hydrostatic stress, and given only the displacement field, the hydrostatic stress field should only be determinate to within a constant. Furthermore, as mentioned in sections 2.2 and 3.1, due to the near incompressibility, even in solving the forward problem, care is needed in choosing the interpolation functions to avoid instabilities.

A simple spatial regularization scheme is adopted, where the hydrostatic stress is weakly enforced to be finite and smooth. We solve the following least-squares minimization problem by adding regularization terms penalizing the L^2 norms of the hydrostatic stress and its gradient to the objective function, which is subjected to be minimized with respect to the shear modulus and hydrostatic stress.

$$\arg \min_{\boldsymbol{\mu}, \mathbf{p}} [(\mathbf{K}\boldsymbol{\mu} + \mathbf{G}\mathbf{p} - \mathbf{f})^T (\mathbf{K}\boldsymbol{\mu} + \mathbf{G}\mathbf{p} - \mathbf{f}) + \beta_1 \mathbf{p}^T \mathbf{p} + \beta_2 (\mathbf{G}_s \mathbf{p})^T (\mathbf{G}_s \mathbf{p})] \tag{24}$$

where β_1 and β_2 are regularization parameters and $\mathbf{G}_s$ is a differential operator in space. If we choose to apply different directional smoothings for distinct directions, it is achieved simply by decomposing single differential operator into the terms for each direction. For example, in a 2D problem,

$$\beta_2 (\mathbf{G}_s \mathbf{p})^T (\mathbf{G}_s \mathbf{p}) = \beta_x (\mathbf{G}_x \mathbf{p})^T (\mathbf{G}_x \mathbf{p}) + \beta_y (\mathbf{G}_y \mathbf{p})^T (\mathbf{G}_y \mathbf{p}). \tag{25}$$

Equation (25) makes it possible to apply separate smoothing in the x and y directions by choosing β_x and β_y non-identically. After minimization, we obtain the system of equations to
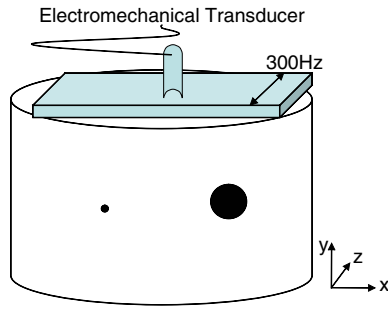
Figure 12. Schematic view of MR experiment set-up for imaging propagating shear waves in a test phantom.

be solved for $\boldsymbol{\mu}$ and $\mathbf{p}$,

$$\begin{bmatrix} \mathbf{K}^T\mathbf{K} & \mathbf{K}^T\mathbf{G} \\ \mathbf{G}^T\mathbf{K} & \mathbf{G}^T\mathbf{G} + \beta_1\mathbf{I} + \beta_x\mathbf{G}_x^T\mathbf{G}_x + \beta_y\mathbf{G}_y^T\mathbf{G}_y \end{bmatrix} \begin{bmatrix} \boldsymbol{\mu} \\ \mathbf{p} \end{bmatrix} = \begin{bmatrix} \mathbf{K}^T\mathbf{f} \\ \mathbf{G}^T\mathbf{f} \end{bmatrix}, \tag{26}$$

which is now used in place of equation (14).

The shear modulus reconstruction algorithm with the stabilization of the hydrostatic stress is tested on the case involving multiple inclusions, which was described in section 3.2. Equation (26) is solved for $\boldsymbol{\mu}$ and $\mathbf{p}$ with taking the regularization parameters to be $\beta_1 = 10^{-11}, \beta_x = 10^{-3}, \beta_y = 10^{-2}$. The result for the case using the exact finite element forward solution data downsampled to the inverse problem mesh is shown in figure 11(b). In comparison to the result without the pressure smoothing, shown in figure 9(b), the artefacts are significantly reduced, but the reconstructed values for the shear modulus are still good. Finally, figures 10(a) and (d) show the reconstructed hydrostatic stress fields from the inversion algorithm with and without including the stabilization of the hydrostatic stress field. In comparison to that computed in the forward solution, shown in figure 10(b), the smoothed result is closer, and, moreover, does not contain the artefacts leading to artefacts in the reconstructed shear modulus.

4. Shear modulus reconstruction from MR measured data

The direct inversion algorithm is applied to reconstruct the shear modulus distribution from the MR measured displacement data of an inhomogeneous test phantom, which is from the same experiment as described in Romano *et al* (2000) and is provided by R L Ehman's group from the Mayo Clinic. A gelatine phantom having two different concentrations of agarose was used to mimic normal soft tissue with abnormal hard inclusions. Two cylindrical shape inclusions with 3.5% agarose concentration acted as hard inclusions while the 1.5% agarose concentration in the background represented normal soft tissue. The exact shear modulus values of the background and inclusions are pre-estimated with the local frequency estimation (LFE) method (Manduca *et al* 1996) by Ehman's group at the Mayo Clinic using two homogeneous test phantoms with agar-gel concentrations identical to this experiment. The shear modulus of the background is estimated to be 20 ($\pm$3) kPa and the stiff inclusion is estimated to be 130 ($\pm$10) kPa (Romano *et al* 2000). The sizes of the inclusions were 16 mm and 3 mm in diameter each. Figure 12 shows the schematic view of the experimental set-up. The test phantom had a cylindrical shape with a diameter of 135 mm and a height of 110 mm. A 300 Hz sinusoidal excitation was applied on top surface of the phantom to generate propagating shear waves. A phase-contrast MRI sequence, having special additional motion
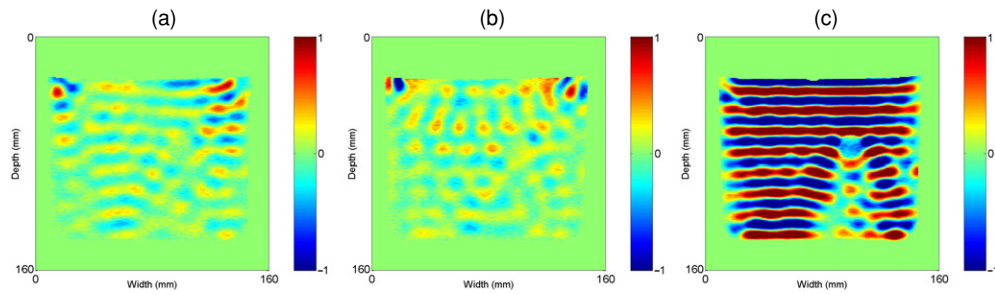
Figure 13. Extracted displacement data used for shear modulus reconstruction. 300 Hz components were extracted using the temporal Fourier transform. (a), (b) and (c) represent x, y and z directional components with relative scale.

encoding, was used to image the propagating waves at the Mayo Clinic (Muthupillai *et al* 1995).

While 300 Hz excitation was applied along the Z-direction using a contact plate operated by the electromechanical transducer, all three directional components of the propagating shear waves were recorded using a 3D echo gradient technique in the XY planes. The size of the imaging plane was 160×160 mm with 256×256 pixels. A total of 16 planes of 2 mm thickness along the Z-direction were imaged and each plane had 4 different images in time. The total dimension of the image data, therefore, is $256 \times 256 \times 16 \times 4 (x \times y \times z \times t)$. See Romano *et al* (2000) for details about the experimental set-up and the result from their algorithm.

Although all three components of displacements were measured in the 3D space, we confined our problem to 3D measurements in a 2D plane. That is, we use all three components of displacements; however, the problem is considered as a 2D plane problem neglecting gradients in the displacement components in the Z direction. In this case, this is reasonable due to the symmetry of the experimental set-up, and it was also observed in the data for the plane considered that the variations of the displacements along the Z-axis were relatively small. We chose the sixth plane among all 16 planes along the Z direction and reconstructed the shear modulus distribution on this plane.

First, a Fourier transform along the temporal dimension is executed to extract the 300 Hz frequency components of the displacements. Figure 13 shows all three extracted components of the displacement data. The values in figure 13 are scaled displacements, which are proportional to the measured phase shift from the phase-contrast MRI technique (Muthupillai *et al* 1995). It is sufficient to use the normalized displacement components without calculating exact values since the relation between elastic properties and displacements is linear in our current model. Figure 13 shows that the Z-component of the displacement is dominant, as expected due to the excitation and the symmetry.

We use the entire 256 by 256 pixel data of MR measured displacements in the shear modulus reconstruction. The inverse finite element discretization is performed using the same base functions for the hydrostatic stress, shear modulus and displacement as we used for all previous tests. Thus, for this problem, we have 196 608 ($256 \times 256 \times 3$) equations and 130 050 ($255 \times 255 \times 2$) unknowns. Since we have more equations than unknowns, the assumption in section 2.3 that the hydrostatic stress and shear modulus on the domain boundary elements are identical to their neighbouring elements is unessential in this case. We also use multiple overlapped sub-domains to decrease the size of the problem for increasing the calculation speed and reducing the possible discrepancies in the reconstructed values between sub-domains. A
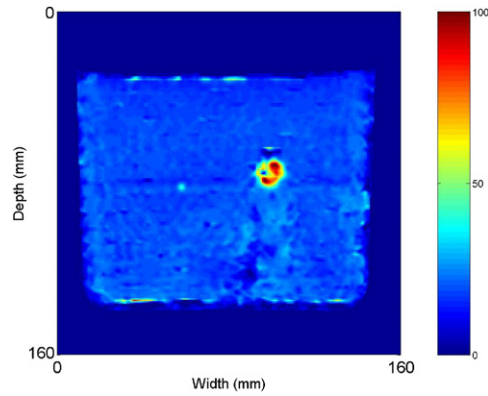
Figure 14. Shear modulus reconstruction from MR data with averaging derivative method (in kPa).
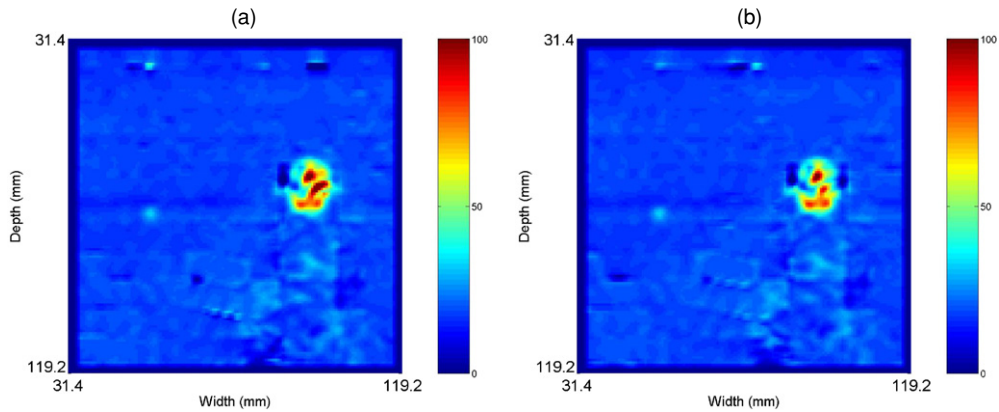

Figure 15. Shear modulus reconstruction with optimization smoothing with all three directional components (a) and with two components after recovering the unknown directional component (b) (in kPa).

total of 784 sub-domains with 20×20 elements are used for the whole domain reconstruction. Each sub-domain is overlapped with neighbouring domains to increase the uniformity of shear modulus on their boundaries. In addition, we assumed the density to be 1000 kg m^{-3}, and we do not apply any regularization to the hydrostatic stress in this case.

Figures 14 and 15 show reconstruction results using two different methods for computing the derivatives of the displacement data. In the first case (figure 14) the method of averaging derivatives, which is based on statistical analysis for computing derivatives of noisy data, proposed by Anderssen and Hegland (1999), is used to compute the displacement gradients in (11). In this method, the derivatives are obtained using the averaged values in space and the size of averaging sets acts like a regularization parameter. The most outstanding benefit of this method is that it does not increase the variance of the derivatives. In this case, the window size used for computing the average derivatives was taken to be 7 by 7 pixels. A variation on this method is used by McLaughlin *et al* (2006) to compute derivatives for reconstructing shear stiffness from the same experiment, but using the Helmholtz approximation. They use a hybrid method that combines the averaging scheme with a median scheme, where they adaptively

choose a method for computing the derivatives based on the signal-to-noise ratio. They also use both the displacement and phase information. Herein, only the displacement information is used with a fixed window size for computing the derivatives. In figure 14, the large 16 mm diameter inclusion is well detected at the correct location and with the correct value of shear modulus. While the small 3 mm diameter inclusion is clearly observable, the value of the reconstructed shear modulus is underestimated as about 40 kPa versus the correct value of about 130 kPa. The reconstructed value is still about twice the background, making it detectable. The reason for the underestimating is the smoothing that results in taking the average derivatives, and the fact that the size of the small inclusion is only about 4–5 pixels across. Another interesting region of the reconstructed image is the region directly behind the inclusions, where the wave motion is significantly altered, as can be seen in figure 13. The region behind an inclusion is difficult to reconstruct using the standard methods based on the Helmholtz equation, and typically results in a very noisy reconstruction in that region. To overcome this limitation, special filters are usually applied to eliminate the noise in such a region (see, for example, Manduca *et al* 2003). However, the use of such filters could also result in missing inclusions behind other inclusions. In this work, no special filter is used in this region, and a good reconstruction is obtained with little noise. This is partially because the Helmholtz equation is not a good approximation in this region due to the heterogeneity. Although the measured displacements do not satisfy the Helmholtz equation in this region, they do satisfy the full governing equations of elasto-dynamics fairly well. Additionally, this region is difficult to reconstruct because of a lower signal-to-noise ratio.

In figure 15, reconstructions using the displacement data smoothed by minimizing the function in equation (15) are shown. Since equation (15) solves the minimization problem using the measured displacements on the whole domain, only the interior region could be considered because of singularities arising outside the phantom boundaries where the gradients are zero. Thus, we exclude those regions and only count the interior 141×141 pixels and use a total of 121 sub-domains having 20×20 size for the recovery. The same values for α_1, α_2 and α_3 were used here as in the prior examples (i.e. 1000, 0.01 and 10, respectively).

Although the measurement of the displacements for all three directions using MRI is possible, it takes three times longer than a single component measurement. We committed the following test to estimate the performance of the smoothing method proposed in equation (15) for overcoming this drawback. In figure 15(a) all three components of the displacement are input into the smoothing algorithm, which finds a set of smooth components that are nearly divergence free and close to the measured displacements. In figure 15(b), only the Y and Z components are used, and the X component together with smooth Y and Z components are obtained using the divergence free and smooth conditions. Interesting, there is little difference between the results using all three displacement components and that using only two. This is a very promising result because it indicates that only two components may be needed, which is less costly than measuring all three components. The results are similar to that obtained with the averaging derivative method. The large inclusion is well captured with close to the correct shear modulus. The small inclusion is observable, has an underestimated shear modulus as in the averaging derivative case and is slightly less resolved. Finally, it should be noted that some additional filtering or post-processing could be used to further improve the image; however, in this paper, we wanted to demonstrate the algorithm by itself and show the unfiltered results.

5. Conclusions

This paper presents a finite element based algorithm for directly reconstructing the shear modulus and hydrostatic stress fields, a sensitivity analysis to indicate the detectability of

inclusions, and some reconstruction results. The algorithm presented has the advantages of not requiring iterations and being suitable to use on sub-regions of the domain, making the algorithm relatively fast compared to other finite element based algorithms. The formulation includes the gradient of the hydrostatic stress and shear modulus terms, which are frequently neglected in reported algorithms. The formulation also weights all the data equally, although unequal weights could also be used if information about the accuracy of the measurements with position and degree of freedom were known. The primary disadvantage of the algorithm is the need to differentiate the data once, which requires a smoothing operation prior to using the data or special methods for differentiating noisy data to avoid large errors due to any noise that may be present in the data.

The mesh convergence and sensitivity study provide useful information regarding modelling error and detectability of inclusions by inverse algorithms. A key finding is that the detectability of inclusions in 2D grows proportional to the area and slightly less than linearly (exponent of 0.8) with the contrast ratio between the background and inclusion. We are currently investigating detectability for 3D inclusions, and will report that work in a later paper.

The inversion algorithm presented was tested on a series of cases involving synthetic data that were generated with a forward finite element analysis on a fine discretization that was then downsampled onto a coarser mesh for use in the inversion algorithm. The coarser mesh represented a more realistic discretization on which measured data could be provided and also allows the inversion algorithm to be tested on data generated from a model different from that on which the inversion algorithm is based. Several cases involving a single cylindrical inclusion and one case involving three inclusions of varying shapes and sizes are considered. The algorithm performs well in detecting the inclusions and capturing the correct values of the shear modulus, but significant artefacts are also present in the solution. These artefacts were shown to result from the instability in reconstructing the hydrostatic stress field. An improved algorithm that includes stabilization of the hydrostatic stress field is presented and successfully removes most artefacts caused by the instabilities in the hydrostatic stress field.

Results from measured data using MR elastography on a tissue mimicking phantom are also presented. This method successfully detects an inclusion with 3 mm in diameter from MR measured displacement images with 0.63×0.63 mm^2 pixel size resolution. Although MR elastography can provide all three components of the displacement field, the optimal smoothing method presented makes it possible to find the third component from two measured components using the property that soft tissue is relatively incompressible. This method can reduce the data acquisition time of MRI without losing the quality of the reconstructed shear modulus. The result is compared with the case using all three measured displacement components.

Finally, this algorithm can be extended to the transient case, which is the subject of a future paper. It is expected that with time dependent data, an improved solution may be obtained because of the richer data set, not only in space, but also in time.

Acknowledgments

References

Anderssen R and Hegland M 1999 For numerical differentiation, dimensionality can be a blessing! *Math. Comput.* **68** 1121–41

Barbone P and Bamber J 2002 Quantitative elasticity imaging: what can and cannot be inferred from strain images *Phys. Med. Biol.* **47** 2147–64

Bercoff J, Chaffai S, Tanter M, Sandrin L, Catheline S, Fink M, Gennisson J-L and Meunier M 2003 *In vivo* breast tumor detection using transient elastography *Ultrasound Med. Biol.* **29** 1387–96

Brezzi F and Fortin M 1991 *Mixed and Hybrid Finite Element Methods* (New York: Springer)

Catheline S, Sandrin L, Gennisson J L, Tanter M and Fink M 2000 Ultrasound-based non-invasive shear elasticity probe for soft tissue *Proc. IEEE Ultrason. Symp.* pp 1799–1801

Catheline S, Wu F and Fink M 1999 A solution to diffraction biases in sonoelasticity: the acoustic impulse technique *J. Acoust. Soc. Am.* **105** 2941–50

Doyley M, Weaver J, Van Houten E, Kennedy F and Paulsen K 2003 Thresholds for detecting and characterizing focal lesions using steady-state MR elastography *Med. Phys.* **30** 495–504

Dutt V, Kinnick R R, Muthupillai R, Oliphant T E, Ehman R L and Greenleaf J F 2000 Acoustic shear-wave imaging using echo ultrasound compared to magnetic resonance elastography *Ultrasound Med. Biol.* **26** 397–403

Fung Y C 1981 *Biomechanics: Mechanical Properties of Living Tissues* (New York: Springer)

Hughes T J R 1987 *The Finite Element Method: Linear Static and Dynamic Finite Element Analysis* (Englewood Cliffs, NJ: Prentice-Hall)

Konofagou E and Ophir J 1998 A new elastographic method for estimation and imaging of lateral displacements, lateral strains, corrected axial strains and Poisson's ratios in tissues *Ultrasound Med. Biol.* **24** 1183–99

Krouskop T, Wheeler T, Kallel F, Garra B and Hall T 1998 Elastic moduli of breast and prostrate tissues under compression *Ultrason. Imaging* **20** 260–74

Lerner R M, Parker K J, Holen J, Gramiak R and Waag R C 1988 Sono-elasticity: medical elasticity images derived from ultrasound signals in mechanically vibrated targets *Acoust. Imaging* **16** 317–27

Malvern L E 1969 *Introduction to the Mechanics of a Continuous Medium* (Englewood Cliffs, NJ: Prentice-Hall)

Manduca A, Lake D S, Kruse S A and Ehman R L 2003 Spatio-temporal directional filtering for improved inversion of MR elastography images *Med. Image Anal.* **7** 465–73

Manduca A, Muthupillai R, Rossman P J, Greenleaf J F and Ehman R L 1996 Image processing for magnetic resonance elastography *SPIE Med. Imaging* **2710** 616–2

McCracken P J, Manduca A, Felmlee J P and Ehman R L 2005 Mechanical transient-based magnetic resonance elastography *Magn. Reson. Med.* **53** 628–39

McKnight A, Kugel J, Rossman P, Manduca A, Hartmann L and Ehman R L 2002 MR elastography of breast cancer: preliminary results *Am. J. Roentgenol.* **178** 1411–17

McLaughlin J R, Renzi D, Yoon F-R, Ehman R L and Manduca A 2006 Variance controlled shear stiffness images for MRE data *IEEE Int. Symp. on Biomedical Imaging: Macro to Nano* pp 960–3

McLaughlin J R and Yoon J-R 2004 Unique identifiability of elastic parameters from time-dependent interior displacement measurement *Inverse Problems* **20** 25–46

Muthupillai R, Lomas D, Rossman P, Greenleaf J F, Manduca A and Ehman R L 1995 Magnetic resonance elastography by direct visualization of propagating acoustic strain waves *Science* **269** 1854–7

Oliphant T, Manduca A, Ehman R L and Greenleaf J F 2001 Complex-valued stiffness reconstruction for magnetic resonance elastography by algebraic inversion of the differential equation *Magn. Reson. Med.* **45** 299–310

Ophir J, Alam S, Garra B, Kallel F, Konofagou E, Krouskop T and Varghese T 1999 Elastography: ultrasonic estimation and imaging og the elastic properties of tissues *J. Eng. Med.* **213** 203–33

Ophir J, Céspedes I, Ponnekanti H, Yazdi Y and Li X 1991 Elastography: a quantitative method for imaging the elasticity of biological tissues *Ultrason. Imaging* **13** 111–34

Ophir J, Garra B, Kallel F, Konofagou E, Krouskop T, Righetti R and Varghese T 2000 Elastographic imaging *Ultrasound Med. Biol.* **26** S23–9

Parker K J, Huang S R and Musulin R A 1990 Tissue response to mechanical vibrations for sonoelasticity imaging *Ultrasound Med. Biol.* **16** 241–6

Romano A, Bucaro J, Ehman R L and Shirron J 2000 Evaluation of a material parameter extraction algorithm using MRI-based displacement measurements *IEEE Trans. Ultrason. Ferroelectr. Freq. Control* **47** 1575–81

Sarvazyan A 1993 Shear acoustic properties of soft biological tissues in medical diagnostics *J. Acoust. Soc. Am.* **93** 2329–30

Sarvazyan A P, Rudenko O V, Swanson S D, Fowlkes J B and Emelianov S Y 1998 Shear wave elasticity imaging: a new ultrasonic technology of medical diagnostics *Ultrasound Med. Biol.* **24** 1419–35

Sinkus R, Tanter M, Xydeas T, Catheline S, Bercoff J and Fink M 2005 Viscoelastic shear properties of in vivo breast lesions measured by MR elastography *J. Magn. Reson. Imaging* **23** 159–65

Srinivasan S, Krouskop T and Ophir J 2004 Comparing elastographic strain images with modulus images obtained using nanoindentation: preliminary results using phantoms and tissue samples *Ultrasound Med. Biol.* **30** 329–43

Taylor L S, Porter B C, Nadasdy G, Anthony di Sant'Agnese P, Pasternack D, Wu Z, Baggs R B, Rubens D J and Parker K J 2004 Three-dimensional registration of prostrate images from histology and ultrasound *Ultrasound Med. Biol.* **30** 161–8

Tanter M, Bercoff J, Sandrin L and Fink M 2002 Ultrafast compound imaging for 2-d motion vector estimation: application to transient elastography *IEEE Trans. Ultrason. Ferroelectr. Freq. Control* **49** 1363–74

Van Houten E, Doyley M, Kennedy F, Weaver J and Paulsen K 2003 Initial in vivo experience with steady-state subzone-based MR elastography of the human breast *J. Magn. Reson. Imaging* **17** 72–85

Van Houten E, Miga M, Weaver J, Kennedy F and Paulsen K 2001 Three-dimensional subzone-based reconstruction algorithm for MR elastography *Magn. Reson. Med.* **45** 827–37

Van Houten E, Paulsen K, Miga M, Kennedy F and Weaver J 1999 An overlapping subzone technique for MR–based elastic property reconstruction *Magn. Reson. Med.* **42** 779–86

Van Houten E, Weaver J, Miga M, Kennedy F and Paulsen K 2000 Elasticity reconstruction from experimental MR displacement data: initial experience with an overlapping subzone finite element inversion process *Med. Phys.* **27** 101–7

Walz M, Teubner J and Georgi M 1993 Elasticity of benign and malignant breast lesions, imaging, applications and results in clinical and general practice *8th Int. Congress on the Ultrasonic Examination of the Breast* p 56

Wu Z, Taylor L S, Rubens D J and Parker K J 2002 Shear wave focusing and three-dimensional sonoelastography *J. Acoust. Soc. Am.* **111** 439–46